

Machine Learning 3D-resolved prediction of electrolyte infiltration in battery porous electrodes

Abbos Shodiev,^{1,2§} Marc Duquesnoy,^{1,4§} Oier Arcelus,^{1,2§} Mehdi Chouchane,^{1,2} Jianlin Li³ and
Alejandro A. Franco^{1,2,4,5*}

¹Laboratoire de Réactivité et Chimie des Solides (LRCS), CNRS UMR 7314, Université de Picardie Jules Verne, Hub de l'Energie, 15 rue Baudelocque, 80039 Amiens Cedex, France

²Réseau sur le Stockage Electrochimique de l'Energie (RS2E), Fédération de Recherche CNRS 3459, Hub de l'Energie, 15 rue Baudelocque, 80039 Amiens Cedex, France

³Electrification and Energy Infrastructure Division, Oak Ridge National Laboratory, Oak Ridge, TN, 37831 United States

⁴ALISTORE-European Research Institute, Fédération de Recherche CNRS 3104, Hub de l'Energie, 15 rue Baudelocque, 80039 Amiens Cedex, France

⁵Institut Universitaire de France, 103 Boulevard Saint Michel, 75005 Paris, France

§ These authors contributed equally to this work.

*Correspondence: alejandro.franco@u-picardie.fr

Summary

Electrolyte infiltration is one of the critical steps of the manufacturing process of lithium ion batteries (LIB). Along with being the most time-consuming step in manufacturing, electrolyte wetting directly impacts the cell energy density, power density and cycle life. We present here an innovative machine learning (ML) model, based on deep neural networks (DNN), to fast and accurately predict fluid flow in three dimensions, as well as wetting degree and time for LIB electrodes. The ML model is trained on a database generated using a 3D-resolved physical model based on the Lattice Boltzmann Method (LBM). We demonstrate the ML model with a NMC electrode mesostructure obtained by X-ray micro-computer tomography. The extracted pore network from tomography data was also used to train our ML neural network. The results show that the ML model is able to predict the electrode filling process, with ultralow computational cost (few seconds) and with high accuracy when compared with the original data generated with the physical model. Also, systematic sensitivity analysis was carried out to unravel the spatial relationship between electrode mesostructure parameters and predicted infiltration process characteristics, such as saturation dynamics, filling time among others.

The ML model is able to speed up the infiltration predictions by several orders of magnitude compared to the LBM model which usually requires several days of calculation. This paves the way towards massive computational screening of electrode mesostructures/electrolyte pairs to unravel their impact on the cell wetting and optimize the electrolyte infiltration conditions.

KEYWORDS. Lithium Ion Batteries, Electrolyte Infiltration, Cell Wetting, Machine Learning, Lattice Boltzmann Method.

1. Introduction

Lithium ion batteries (LIBs) can provide high energy and power densities with long cycle life,¹ constituting the technology of choice nowadays for electronic gadgets and electric vehicles.² Therefore, the demand for LIB increases rapidly and its cost becomes one of the critical issues to overcome. Generally, the price depends on the battery's cell chemistry and manufacturing process.³ And the electrolyte infiltration in the battery cell is one of the bottlenecks in the manufacturing process.⁴ It is crucial to optimize the electrolyte infiltration as it takes a relatively long time compared to the other manufacturing steps.⁵ Moreover, it can also impact the electrochemical performance of the cell. Indeed, a poor electrolyte impregnation decreases the active surface area (active material/electrolyte interface), and creates an inhomogeneous SEI layer in LIB negative electrodes, which may lead to low energy and power densities, and shorter cycle life.^{6,7,8,9,10}

Despite its importance, it is experimentally challenging to analyze electrolyte flow through the porous electrodes. Several attempts were made to capture the dynamic path of the infiltrating electrolyte by using 2D in-plane imbibition, transmission neutron and X-ray imaging.^{11,12,13} Nevertheless, these studies lack appropriate resolution and detailed information due to the limitations of the techniques. In addition, the experimental results constitute average values, making very challenging the differentiation of the effect of various manufacturing conditions on electrolyte wetting. Moreover, performing high throughput experimental characterizations to unravel parameters interdependencies in the infiltration process is not a trivial task,^{13,14} since the experimental techniques reported in the literature are costly and require sophisticated tools.¹⁵

On the other side, a recent increase in computational power enables performing three dimensional (3D) fluid flow computational simulations to quantify the permeability of complex porous materials and electrolyte penetration, which can be carried out in electrode images obtained by

micro-computer tomography (CT). One of the most prominent tools to evaluate the permeability of 3D mesostructures is the Lattice-Boltzmann Method (LBM).⁷ The strength of this method comes from its mesoscopic nature based on the discrete kinetic theory, which straightforwardly includes biphasic interface dynamics. Thus, the LBM is an accurate numerical method to simulate physical phenomena in realistic electrode mesostructures. Typically, LBM simulations are performed in representative elementary volumes (REVs), where relatively small sub-volumes of the bigger mesostructure are selected, such that the global mesostructural properties are preserved.^{16,17} For the first time, we recently reported this approach to simulate electrolyte infiltration into LIB electrode mesostructures in 3D.⁷ Results arising from LBM simulations are generally accurate, reliable and allow deep physical interpretation of the infiltration process.

Nevertheless, performing routine calculations with LBM remains computationally expensive and time-consuming: typically, 48 to 120 hours are needed for simulating electrolyte infiltration in one electrode, running the code in a supercomputer. Still, LBM constitutes a great tool to produce big data for further analysis (100-300 Gigabytes per electrode), something which is not possible with current experimental tools. Still, the bottleneck of the LBM model is the inability to quickly screen a massive amount of electrode architectures and electrolyte types. Consequently, it remains crucial to speed up the simulation of the electrolyte infiltration process to pave the way towards the computational screening of the impact of electrolyte and electrode properties on the electrolyte infiltration dynamics and therefore envisage autonomous algorithms able to optimize the electrolyte infiltration for low required times.

Meanwhile, Artificial Intelligence (AI) has seen a tremendous rise in the last decade, becoming essential for modern industry and finance, among many other fields.¹⁸ In LIBs, machine learning (ML) techniques have enabled tools that significantly reduce the slow time frames related to trial-

and-error approaches or physics-based simulations for faster and more efficient data assessment.^{19–}
²² Deep Neural Networks (DNNs) are the most popular technique in the AI field due to the good performances they show for modeling complex data structures with many non-linear relationships.^{23–24} Particularly, Convolutional Neural Networks (CNNs), a type of DNN, are a perfect example, having outstanding performances in different applications involving many types of data such as images-to-images translations, image classification, or autonomous driving.^{25–27} Such techniques have also been applied to datasets produced from LBM calculations in the geology domain through images-based prediction to obtain fluid flow properties in porous media.^{16,28,29} They generally consist of supervised regression ML models, which reduce computational costs and predict relevant physical properties such as porosity or permeability from tomography (micro-CT) X-ray images.^{30–32}

In the field of energy storage, DNN architectures have also become very popular to accelerate physical-based simulations and reduce trial-and-error efforts to optimize LIBs.³³ Therefore, our aim in this study is to report, for the first time to our knowledge, a ML model based on a multi layers perceptron model (MLP) that can describe the dynamics of the electrolyte infiltration process in 3D, given a particular mesostructure of a LIB electrode and its associated pore-network, while accounting for different external infiltration pressure conditions. The ML model was trained with the data coming from LBM simulations due to the lack of big data from the experimental side, but keeping in mind that the results of the LBM simulations are based on experimentally measured input parameters. Still, it is essential to notice that one more strength of the reported ML model is that it can be adapted for different sources of data (pure experimental or hybrid between experimental and simulated) as far as this concerns the same type of data. The manuscript is divided into three sections: first we present the different processing steps in obtaining the REV

using micro-CT X-ray tomography data coming from our previous work;⁷ then we present the LBM simulation details to generate the data and the adopted MLP architecture; lastly, we present electrolyte infiltration prediction results from our ML model along with detailed sensitivity analysis on the effects of the pore-network properties and LBM simulation conditions on the predicted electrolyte infiltration dynamics. Finally, we discuss why this approach has the potential to pave the way towards fast computational screening of electrode architectures/electrolyte pairs for the accelerated optimization of electrolyte infiltration and LIB manufacturing process as a whole.

2. Computational procedures

Extraction of REV's: From the full tomography dataset of the NMC 94% - CBD 6% electrode, eleven $100 \cdot 100 \cdot 75 \mu\text{m}^3$ sub-volumes of similar porosities were extracted with a maximal relative error of 5 %. The carbon binder domain (CBD) location in the REV's was resolved using an *in house* stochastic algorithm.²²

Individual pore identification: An accurate reconstruction of the three-dimensional pore spaces and the subsequent identification of individual pores was done by the PoroDict library within the GeoDict[®] software using the watershed algorithm. It is known that the surface roughness of 2D images (or 3D voxel data in our case) generally induces over-segmentation in watershed-based methods and many approaches exist to solve it.^{34,35} GeoDict[®] handles this by reconnecting overly segmented pore-fragments back into a single pore only when the shared interface between the pore fragments is larger than a chosen value. For consistency, this interface threshold value is kept constant at 10 % for each of the representative sub-volumes that were extracted and analyzed. Then, their volume, surface area, and surface area of contact with other pores were calculated based on a six neighbors approach.³⁶ Compared to other pore-network modelling approaches,^{37–39} where the pores are approximated as spheres and cylindrical throats, the watershed algorithm identifies individual pores by labeling every voxel in the pore phase. This is especially useful when

setting a one-to-one correspondence between the pore-wise labeled volumes and other voxel-based volumetric data coming from LBM simulations.

LBM simulations: Simulations were carried out using the open-source Palabos library version 1.0.⁴⁰ The model simulates the streaming and collision of particles on a grid. All the simulations are in the laminar flow regime. The Navier-Stokes macroscopic kinetic theory was applied to describe fluid in the bulk flow at the mesoscopic level. Further details of the model and its description can be found in our previous LBM publication.⁷ All the input parameters such as the density, the fluid contact angle with the solid phase, the viscosity, the surface tension and the sizes of simulation boxes are given in Table 1. After, the outputs from the Palabos library were further treated using NumPy⁴¹ with the PyVista library⁴² in order to obtain the individual pore-resolved saturation curves.

ML model: In this study, a sequential architecture is implemented to model the saturation curve values \bar{S} and the times of filling (T_{f0} and T_{f1} as seen in Figure 1D) for every pore in the tomographic REV's. The developed architecture follows a neural network-based model known as a MLP. The Python libraries, Tensorflow and Keras, are used in the backend to complete the architecture within a 3.7 version of Python. After training the modeling function, a sensitivity analysis is applied to analyze the effect of the input parameters on the uncertainty of the outputs. The architecture of the MLP comprises five hidden layers, with 80 nodes each, and one output layer containing 7 nodes. While no specific rule exists for selecting DNN hyperparameters,⁴³ this architecture was sufficient to fit the training data correctly and to obtain trustable predictions as shown in the results section.

The LBM model simulations were performed using an Intel® Xeon® E5-4627 Cache @ 3.30 GHz with 264 GB of RAM. Each simulation took approximately between 48 and 120 hours, depending on the input pressure parameter. The NN models' training took around 10 minutes by using 48 processors Intel® Xeon® Silver 4116 CPU @ 2.10 GHz with 64 GB of RAM.

Figure 1 illustrates the workflow that was used in this work. The details of the data extraction procedure of pore-resolved saturation curves and the ML model are given in the supplemental information.

A 3D illustration

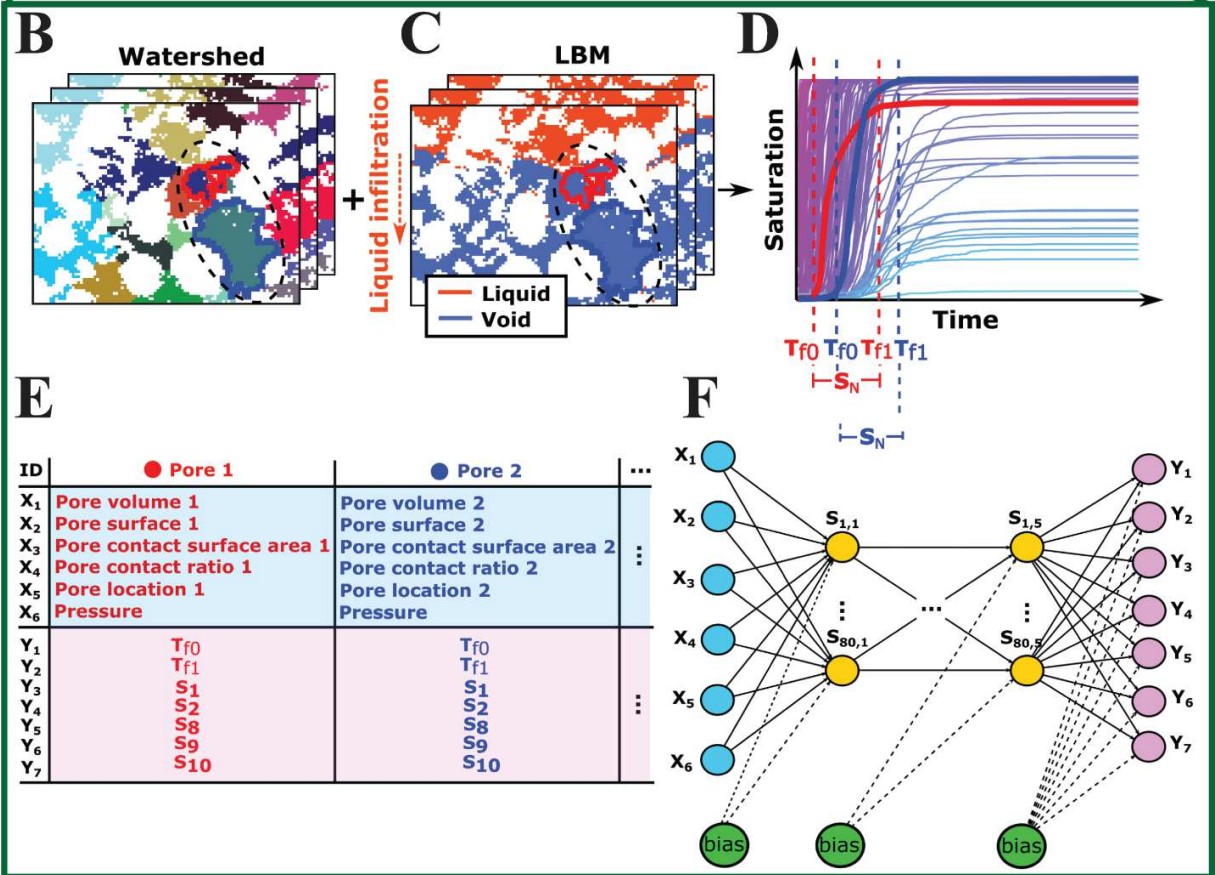
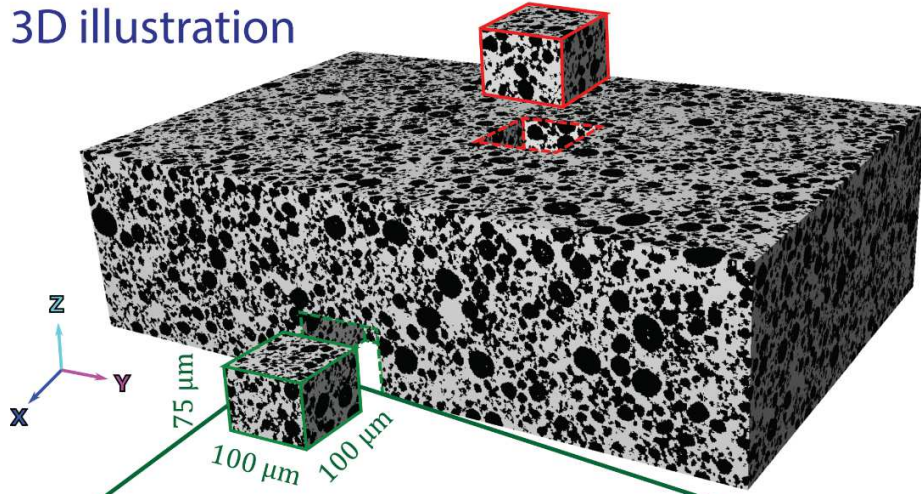


Figure 1. Summary of the data processing steps to be used as inputs in the ML model. (A) 3D micro-CT X-ray tomography data, colored rectangular parallelepipeds represent two examples of the different REV's that were extracted. (B) (left) Results from the watershed segmentation process, (C) (middle) volume data

from LBM simulations with voxels labeled as liquid (orange), void (blue), and solid (white). (D) (right) Individual pore-resolved saturation curves. For clarity, two pores (blue and red) were highlighted, spanning the same spatial regions between the watershed and LBM voxel data. The respective pore-resolved saturation curves are also shown, alongside their relevant features (\bar{S} , T_{f0} , and T_{f1}). (E) Structure of the data used for the training of the NN, columns enumerate each pore, while rows are divided into the inputs $(X_i)_{(i \leq 6)}$ (blue shaded region) and outputs $(Y_i)_{(i \leq 7)}$ (red shaded region). (F) Architecture of the neural network used for training, nodes in blue (red) represent the input (output) layers, respectively. Nodes in yellow represent the hidden layer nodes $S_{j,k}$ where k is the layer index, and j is the node index. Nodes in green represent the bias that is applied to each hidden layer.

3. Discussion

3.1. Machine learning prediction

The evaluation of the electrolyte infiltration dynamics was done by extracting the relevant features of pore resolved saturation curves as shown in Figure 1D. Specifically, we extracted the values of the times at which the pore filling starts (T_{f0}) and stops (T_{f1}), as well as the saturation values associated to ten in-between evenly spaced time steps, as the outputs of the MLP. The set of saturation points are defined as $\bar{S} = \{S_1, S_2, S_3, S_4, S_5, S_6, S_7, S_8, S_9, S_{10}\}$.

Figure 2 displays the critical features for the training and validation of the MLP. The complete dataset is randomly split into the training and testing dataset containing 80 % and 20 % of the total data, respectively. Figure 2A represents the evolution of the loss values (MSE) for the training data (80% of the total amount of data) and the validation data (the remaining 20%) during the training step of the MLP over 1000 training cycles. Figure 2B shows the average R^2 scores for the model compared with the mean square error (MSE) between the initial saturation curve and its discretization to define the saturation values outputs. In order to obtain a compromise between the global accuracy of the MLP and the error between the saturation curves and their associated discretized values, we successively retrained the MLP model after removing those saturation value outputs that were not properly fitted, thus reducing the number of outputs in the model. Particularly, this compromise is met by selecting $\bar{S} \setminus \bar{S}_{3-7} = \{S_1, S_2, S_8, S_9, S_{10}\}$ as the outputs of the

MLP, along with T_{f0} and T_{f1} (as shown in Figure 1E-F). Figure 2C and Figure 2D display regression plots comparing the predicted values from the MLP model and the actual values from the LBM simulations for the testing dataset, for the time at which the pore-filling starts (T_{f0}) and stops (T_{f1}), respectively.

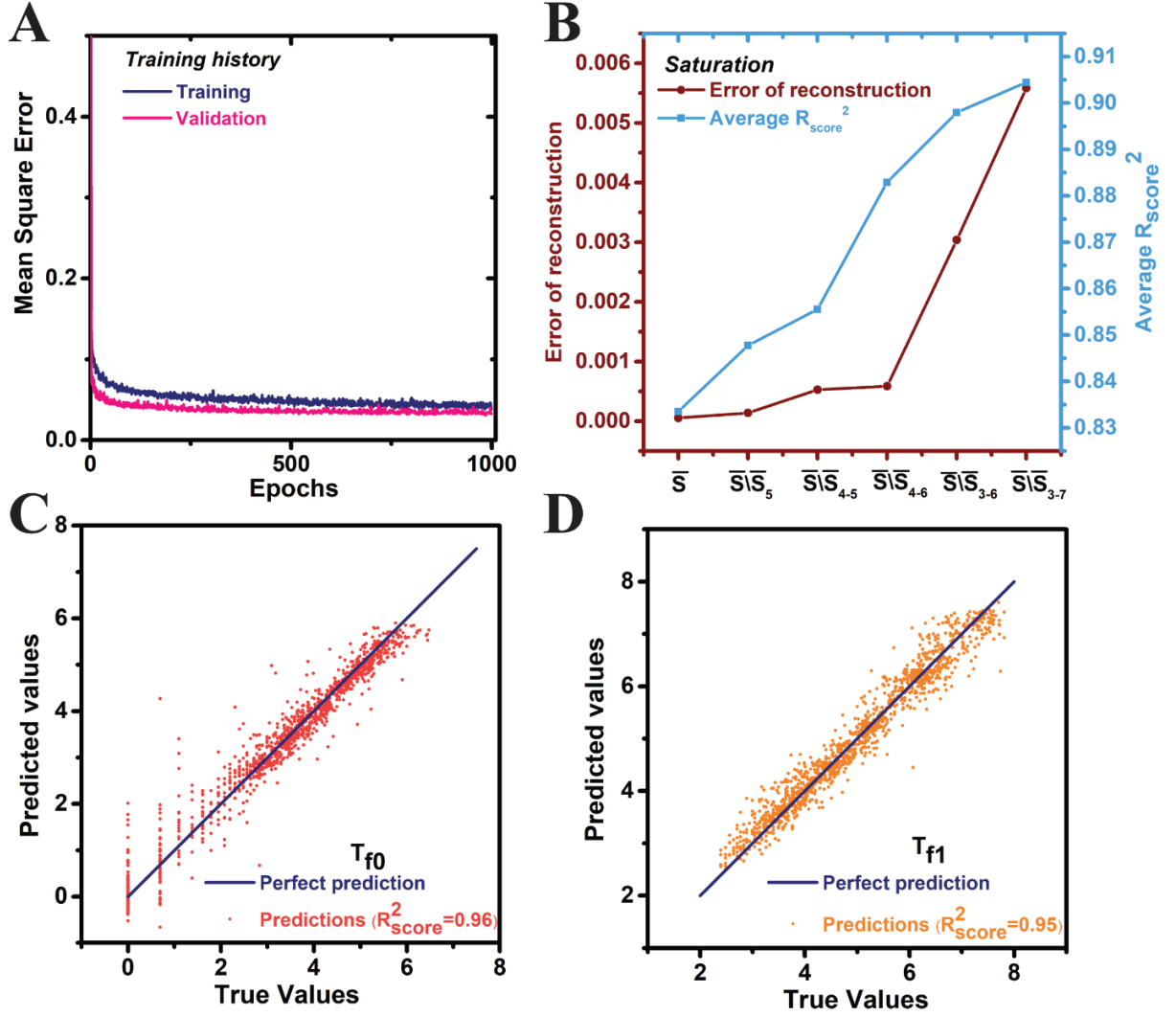


Figure 2. (A) MSE of the training and validation of the neural network, (B) R^2 scores (blue) and the MSE of the saturation curve reconstruction (garnet) as function of the set of saturation value ($\bar{S} \setminus \bar{S}_i$) outputs predicted by the model, (C) Prediction of the starting times for electrolyte filling of individual pores (T_{f0}) and (D) Prediction of the full wetting times (T_{f1})

3.2. Comparison of LBM simulation and prediction based on ML

As mentioned above, our trained MLP can accurately predict the saturation, initial electrolyte entering and fully wetting time at an individual pore in the structure for the test dataset. In order to further compare and contrast our model, an additional REV was used, whose pore-network was not part of neither the training nor testing datasets. After inputting the parameters of the brand-new pore-network in our MLP, the overall saturation curves were reconstructed from the obtained outputs, as shown in Figure 3. The obtained results closely match the saturation curves obtained with LBM, which gives a hint of the ability our ML model to perform well in a variety of electrode mesostructures.

Five different applied pressures were also used as input parameters to study and predict their effect on electrolyte penetration. Again, Figure 3 shows the overall saturation curves simulated by LBM, and predicted by our MLP for different applied pressures. Generally, all saturation curves for both real and predicted cases show an asymptotic growth rate where the saturation curve increases steeply and slows down while it reaches the convergence point. Also, the wetting time for the electrode increases as applied pressure decreases for both real and predicted cases. Furthermore, the lower the applied pressure, the lower the overall saturation will be and the longer it will take to reach the convergence point. The saturation curves for real (LBM simulated) cases under the applied pressures p_8 , p_4 and p_2 tend to rise monotonically and reach complete wetted conditions. For the lower pressure values (p_1 and $p_{0.5}$), the electrode wetting degrees are only 60% and 25%, respectively. In addition, the penetration rate, *i.e.* the rate at which the saturation will reach its convergence point, is slower for p_1 and $p_{0.5}$ compared to higher applied pressures. The predicted (MLP based) saturation curves agree with those from LBM simulated results, especially at high applied pressures where the predictions are extremely precise. In essence, the vital part is that the MLP can closely match the general simulation trends and is also able to precisely predict

converging points, where the saturation degrees predicted by our MLP closely match those obtained by LBM simulations for high applied pressure inputs.

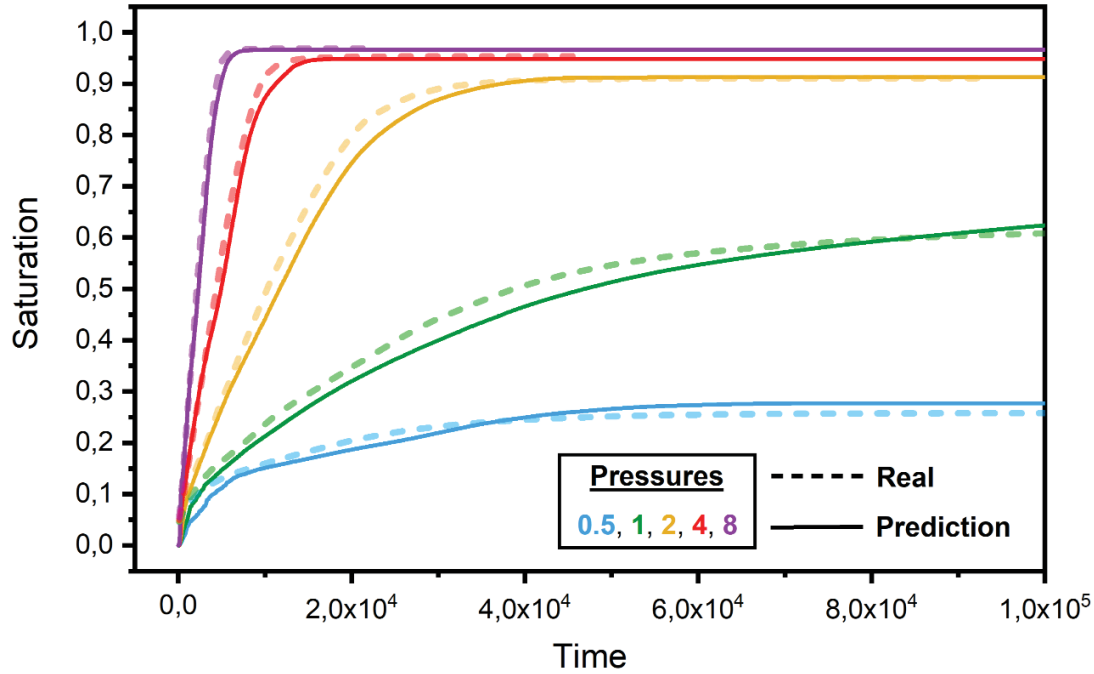


Figure 3. Saturation profile of liquid electrolyte from real (LBM simulated) and predicted (NN based) in the NMC 94% - CBD 6% cathode with various applied pressures.

Our model also allows following the electrolyte wetting process in 3D, since its outputs depend on spatially resolved pore-networks. Figure 4 shows the temporal evolution of the saturation degree of individual pores in the electrode mesostructure. It is known that electrolyte flows through the porous electrode due to the pressure difference between the electrolyte and air phases, known as capillary forces, while local resistance forces drive the electrolytes path within the porous electrode. Usually, the electrolyte is always directed towards larger pores, as shown in our previous the LBM simulations.⁷ Figure 4 shows an excellent agreement between the MLP prediction and physical-based LBM model, in the path that the electrolyte takes within the porous electrode. There is a slight deviation at time step $1 \times 10^4 \text{lu}$, but the difference disappears at the converging point. The

corresponding videos of the filling process as predicted by LBM and ML are provided in supplemental information.

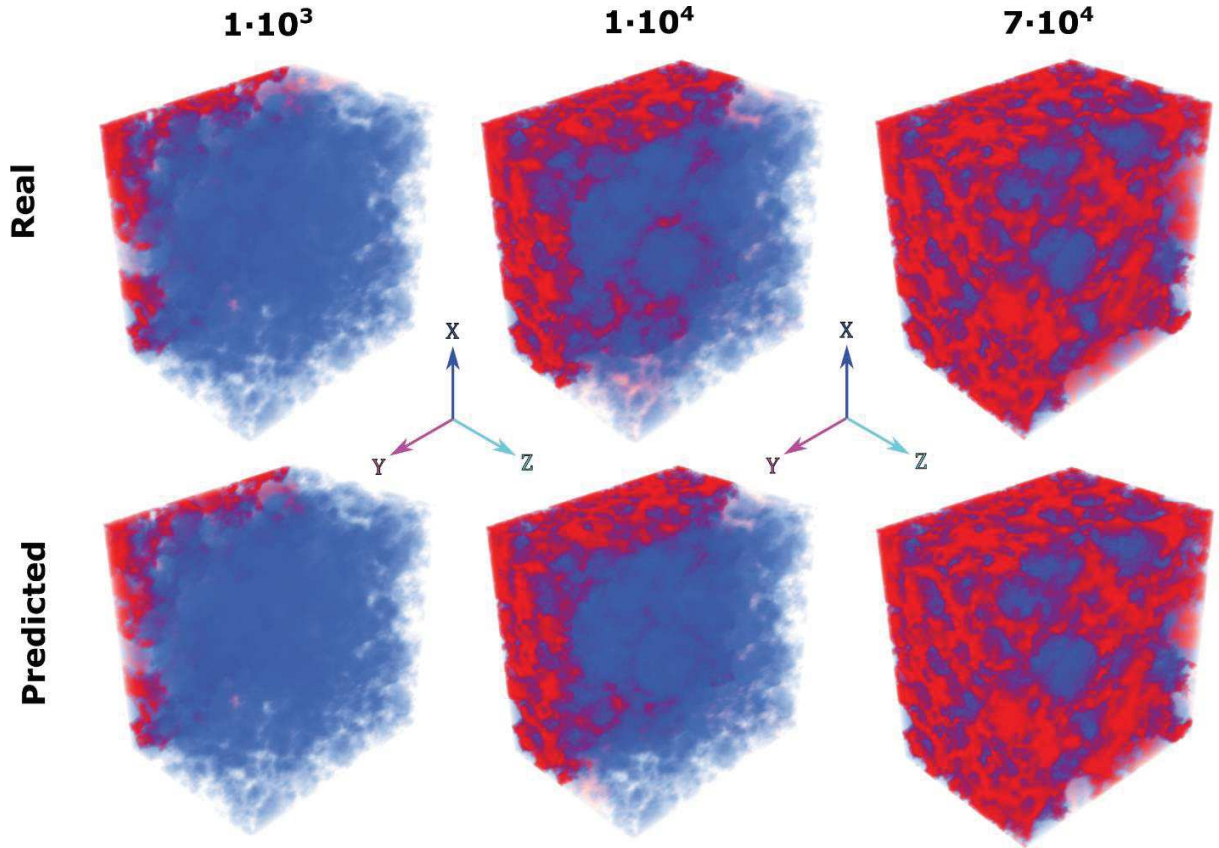


Figure 4. The wetting process visualization (electrolyte in red color) from real (LBM simulated) and predicted (MLP based) for the NMC 94% - CBD 6% electrode (blue) at different time steps. The electrolyte inlet is the yz plane at $x = 0$.

3.3. Parameters influencing the saturation and their physical interpretation

Performing a sensitivity analysis of computational models is a clear and straightforward way to assess how the outputs of a model vary as a function of their inputs. In this work the *Sobol* indexes were extracted in order to evince the individual and total impact that the input parameters of the MLP model have on the seven outputs that we aim to predict, *i.e.* T_{f0} , T_{f1} and the saturation values \bar{S} . Additionally, the Sobol indexes corresponding to the initial ($S_{f0} = \{S_1, S_2\}$) and final ($S_{f1} = \{S_8, S_9, S_{10}\}$) saturation values are averaged out, which allows condensing the results in order to

facilitate their physical interpretation (Figure 5). Let the decomposition of the total variance for one specific output (named Y) according to the Sobol decomposition be expressed as

$$V_{ar}[Y] = V(Y) = \sum_{i=1}^n V_i + \sum_{1 < i,j < n} V_{i,j} + \dots + V_{1,\dots,n} \quad (1)$$

where V_i is the conditional variance for Y over knowing X_i , and $V_{i,\dots,n}$ are the rest of conditional variances knowing different input parameters.

The Sobol indexes are the partial variances normalized by the total variance of the output, they are noted as $(Sob_i)_{(i \leq n)}$ and they are comprised between 0 and 1 (Eq. 11). They represent the individual effects (1st order Sobol indexes) of each input parameter:

$$Sob_i = \frac{V_i}{V} = \frac{V[E[Y \vee X_i]]}{V[Y]} \quad (2)$$

In this study, the Sobol index depends on the chosen output $(Y_j)_{(j \leq 7)}$, meaning that the equation above can be simplified as

$$Sob_{i,j} = \frac{V_i}{V_j} = \frac{V[E[Y \vee X_i]]}{V[Y_j]} \quad (3)$$

where $E[Y \vee X_i]$ is the conditional expectation of Y_j giving X_i .

By successively adding higher order terms to the indexes, we obtain the total effect for each input parameter

$$Sob_{T_i} = Sob_i + \sum_{i \neq j} Sob_{ij} + \sum_{j < k, i \neq j, i \neq k} Sob_{ijk} + \dots \quad (4)$$

where the different Sobol indexes Sob_{ijk} are related to the combination of various input parameters. Such indexes are calculated according to the Saltelli sampling method.^{44,45} The latter global approach is very popular to obtain convergences when the number of samples varies significantly and represents the entire space of input parameters, whereas random sampling approaches may perform meaningless evaluations of sensitive indexes. Therefore, the Saltelli method extends the size of input parameters combinations for the resulting calculations, which are uniformly distributed over the full input parameters space. The variances calculated from Eq. 10 to Eq. 12 can be described as projections along the different ranges of input parameters. In this study, a batch of 14000 samples is used to evaluate the Sobol indexes for each output of the MLP.

Figure 5 shows the 1st order Sobol indexes regarding all possible combinations between inputs (geometrical properties of the pores and applied pressures) and outputs (T_{f0} , T_{f1} , S_{f0} and S_{f1}) in this study. We can see that the initial pore filling time (T_{f0}) highly depends on the pore volume with a Sobol index of 0.7 followed by the pore total surface area and its location with Sobol indexes of 0.3. The total wetting time of the pore (T_{f1}) is also influenced mainly by these three parameters. The pore volume has a major effect with a Sobol index of 0.6 and the second biggest factor is the pore surface area with Sobol index 0.4. It is intuitive that the bigger the pore size, the easier it is for the electrolyte to occupy its volume. Also, other geometrical attributes such as pore location and pore surface area play a significant role in the pore filling start time (T_{f0}). Additionally, it is important to mention that all the input parameters have almost the same effect on the saturation values at the end of the pore filling (S_{f1}) with Sobol indexes about 0.45. The onset of saturation S_{f0} is, on the contrary, strongly influenced by the pore location with Sobol index around 0.7.

To sum up, the total electrode's wetting degree strongly depends on the pore network properties and applied pressure. The full wetting time (T_{f1}) is strongly affected by pore size distribution. Thus,

to have optimal electrode mesostructures to reach complete wetting at the shortest possible time, pore size distribution and interconnectivity of the pores must be well designed during the manufacturing. This can be a challenging task with traditional manufacturing process, still it is achievable with alternative techniques such as SPS sintering and 3D printing.^{46,47}

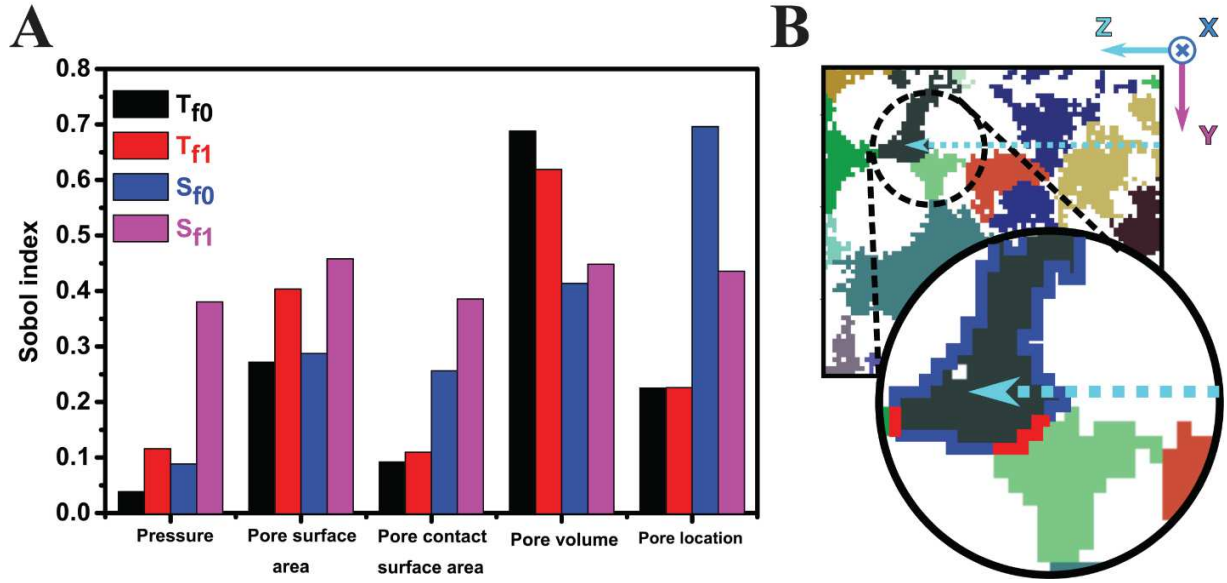


Figure 5. (A) Sobol indexes of the geometrical properties of individual pores and applied pressures, on the outputs T_{f0} , T_{f1} , S_{f0} , and S_{f1} . (B) Slice of the REV illustrating the geometrical properties of individual pores. The zoom region (black circle) illustrates the pore volume (grey zone), pore surface area (blue outline), pore contact surface area (red outline) and pore location (dotted turquoise arrow) of a given identified pore inside the REV.

4. Conclusions

In this work, we present an innovative ML model based on a multi layers perceptron (MLP) architecture, to predict electrolyte infiltration in porous NMC electrodes. The host structure of the NMC porous electrode was obtained experimentally by (micro-CT) X-ray tomographic measurements. The MLP was trained with data coming from physics-based 3D LBM model and extracted pore networks from (micro-CT) X-ray tomography. The neural network prediction results were compared and validated by 3D LBM simulations.

The trained MLP can generalize the flow problems to predict the rate of saturation and filling time in porous electrodes. Moreover, it can predict the direction of the fluid flow, total saturation, and filling time of the electrode accurately. Also, the predictions showed the same asymptotic trend as the physics-based LBM model for the saturation curve. Additionally, a systematic sensitivity analysis was carried out to unravel the spatial relationship between complex electrode pore shape, pore location, pore volume, the connection between other pores and applied external pressure on the overall predicted infiltration process characteristics, such as saturation degrees and filling times, among others.

Besides, the trained MLP accurately predicted examples of varying geometries and applied pressures in less than a second of computation on a desktop computer, while physics-based LBM simulations took several days (2-5) on a server with high computational power. Additionally, our ML model generates only around 10 Mb of data to be compared with the 50 - 200 Gb generated during the LBM simulations, saving data storage space and making post-processing fast and affordable. All the advantages mentioned above allow the model to quickly screen different electrode architectures and possible electrolyte properties as a part of a digital twin of battery manufacturing. Consequently, it serves as a vital tool to optimize the electrolyte infiltration process. Finally, this method can be used further on different domains where fluid flow through porous media takes part.

Table 1. List of input parameters for the LBM simulations

AM 96%-CBD 4% un-calendered tomography	100×100×75 voxels	$100 \times 100 \times 75 \mu\text{m}^3$
Electrolyte denisty	10	$1300 \frac{\text{kg}}{\text{m}^3}$
Gas denisty	1	$1.18 \frac{\text{kg}}{\text{m}^3}$
Contact angle	0.357/1.643	90° ¹³
Surface force (gas-liquid)	0.1	7.28×10^{-2}
t_0	1 <i>lu</i>	$1 \times 10^{-6} \text{s}$
Reynolds number	10^{-3}	10^{-3}
Capillary number	10^{-5}	10^{-5}
Pressure	0.5 p	151 988 Pascal
Pressure	1p	202 650 Pascal
Pressure	2p	405 300 Pascal
Pressure	4p	810 600 Pascal

Contributions: A.S., O.A., M.D. and A.A.F. had the original idea and designed the work plan. A.S., M.D., carried out the modeling. O.A., performed data management. A.S., O.A., M.C. provided inputs. A.S., M.D., OA., J.L. and A.A.F. interpreted the results. A.S., O.A. and M.D. wrote the first version of the manuscript. All the authors edited and reviewed the manuscript. A.A.F. obtained the funding for this research and supervised the work.

Acknowledgements

A.A.F., A.S., M.D. and M.C. acknowledge the European Union's Horizon 2020 research and innovation programme for the funding support through the European Research Council (grant agreement 772873, "ARTISTIC" project). A.A.F. and M.D. acknowledge ALISTORE European Research Institute for partial funding support. A.A.F. and O.A. acknowledge partial funding from the Région Hauts de France and from the European Union's Horizon 2020 research and innovation program under grant agreement No 957189 (BIG-MAP). The authors also thank Markus Osenebrg, André Hilger and Ingo Manke for the support at the P05 synchrotron beamline at DESY at Institute of Applied Materials, Helmholtz-Zentrum Berlin für Materialien und Energie GmbH. The authors acknowledge Emiliano Primo for preparation of the electrodes. A.A.F. acknowledges Institut Universitaire de France for the support. J. L. appreciate the support from the Office of Energy Efficiency and Renewable Energy (EERE) Vehicle Technologies Office (VTO). The research at Oak Ridge National Laboratory (ORNL) is managed by UT Battelle, LLC, for the U. S. Department of Energy (DOE) under contract DE-AC05-00OR22725.

Declaration of competing interest

The authors declare that they have no known competing financial interests or personal relationships that could have influenced the work reported in this paper.

Data and Code availability

All the data and the codes used in the scope of this work will be publicly available on the ERC-ARTISTIC project's website <https://www.erc-artistic.eu>

References

1. Harlow, J.E., Ma, X., Li, J., Logan, E., Liu, Y., Zhang, N., Ma, L., Glazier, S.L., Cormier, M.M.E., Genovese, M., et al. (2019). A Wide Range of Testing Results on an Excellent Lithium-Ion Cell Chemistry to be used as Benchmarks for New Battery Technologies. *J. Electrochem. Soc.* *166*, A3031–A3044.
2. Franco, A.A., Rucci, A., Brandell, D., Frayret, C., Gaberscek, M., Jankowski, P., and Johansson, P. (2019). Boosting Rechargeable Batteries R&D by Multiscale Modeling: Myth or Reality? *Chem. Rev.* *119*, 4569–4627.
3. Borah, R., Hughson, F.R., Johnston, J., and Nann, T. (2020). On battery materials and methods. *Mater. Today Adv.* *6*, 100046.
4. Knoche, T., Surek, F., and Reinhart, G. (2016). A Process Model for the Electrolyte Filling of Lithium-ion Batteries. *Procedia CIRP* *41*, 405–410.
5. Wood, D.L., Li, J., and Daniel, C. (2015). Prospects for reducing the processing cost of lithium ion batteries. *J. Power Sources* *275*, 234–242.
6. Jeon, D.H. (2019). Wettability in electrodes and its impact on the performance of lithium-ion batteries. *Energy Storage Mater.* *18*, 139–147.
7. Shodiev, A., Primo, E., Arcelus, O., Chouchane, M., Osenberg, M., Hilger, A., Manke, I., Li, J., and Franco, A.A. (2021). Insight on electrolyte infiltration of lithium ion battery electrodes by means of a new three-dimensional-resolved lattice Boltzmann model. *Energy Storage Mater.* *38*, 80–92.
8. Pfeifer, K., Greenstein, M.F., Aurbach, D., Luo, X., Ehrenberg, H., and Dsoke, S. (2020). Interaction between Electrolytes and Sb₂O₃-Based Electrodes in Sodium Batteries: Uncovering the Detrimental Effects of Diglyme. *ChemElectroChem* *7*, 3487–3495.
9. Shodiev, A., Primo, E.N., Chouchane, M., Lombardo, T., Ngandjong, A.C., Rucci, A., and Franco, A.A. (2020). 4D-resolved physical model for Electrochemical Impedance Spectroscopy of Li(Ni_{1-x-y}Mn_xCo_y)O₂-based cathodes in symmetric cells: Consequences in tortuosity calculations. *J. Power Sources*, 227871.
10. Chouchane, M., Arcelus, O., and Franco, A.A. (2021). Heterogeneous Solid Electrolyte Interphase in Graphite Electrodes Assessed by 4D-Resolved Computational Simulations. *Batter. Supercaps*, batt.202100030.
11. Schilling, A., Gumbel, P., Möller, M., Kalkan, F., Dietrich, F., and Dröder, K. (2019). X-ray Based Visualization of the Electrolyte Filling Process of Lithium Ion Batteries. *J. Electrochem. Soc.* *166*, A5163–A5167.
12. Weydanz, W.J., Reisenweber, H., Gottschalk, A., Schulz, M., Knoche, T., Reinhart, G., Masuch, M., Franke, J., and Gilles, R. (2018). Visualization of electrolyte filling process and influence of vacuum during filling for hard case prismatic lithium ion cells by neutron imaging to optimize the production process. *J. Power Sources* *380*, 126–134.

13. Davoodabadi, A., Li, J., Liang, Y., Wood, D.L., Singler, T.J., and Jin, C. (2019). Analysis of electrolyte imbibition through lithium-ion battery electrodes. *J. Power Sources* 424, 193–203.
14. Davoodabadi, A., Li, J., Zhou, H., Wood, D.L., Singler, T.J., and Jin, C. (2019). Effect of calendaring and temperature on electrolyte wetting in lithium-ion battery electrodes. *J. Energy Storage* 26, 101034.
15. Hawley, W.B., and Li, J. (2019). Electrode manufacturing for lithium-ion batteries—Analysis of current and next generation processing. *J. Energy Storage* 25, 100862.
16. Santos, J.E., Xu, D., Jo, H., Landry, C.J., Prodanović, M., and Pyrcz, M.J. (2020). PoreFlow-Net: A 3D convolutional neural network to predict fluid flow through porous media. *Adv. Water Resour.* 138.
17. Zhu, J., and Ma, J. (2018). Extending a Gray Lattice Boltzmann Model for Simulating Fluid Flow in Multi-Scale Porous Media. *Sci. Rep.* 8, 1–19.
18. Mistry, A., Franco, A.A., Cooper, S.J., Roberts, S.A., and Viswanathan, V. (2021). How Machine Learning Will Revolutionize Electrochemical Sciences. *ACS Energy Lett.* 39, 1422–1431.
19. Mistry, A., Franco, A.A., Cooper, S.J., Roberts, S.A., and Viswanathan, V. (2021). How Machine Learning Will Revolutionize Electrochemical Sciences. *ACS Energy Lett.* 14, 1422–1431.
20. El-Bousiydy, H., Lombardo, T., Primo, E.N., Duquesnoy, M., Morcrette, M., Johansson, P., Simon, P., Grimaud, A., and Franco, A.A. (2021). What Can Text Mining Tell Us About Lithium-Ion Battery Researchers' Habits? *Batter. Supercaps*, batt.202000288.
21. Kumar, S., Tan, S., Zheng, L., and Kochmann, D.M. (2020). Inverse-designed spinodoid metamaterials. *npj Comput. Mater.* 6, 1–10.
22. Duquesnoy, M., Lombardo, T., Chouchane, M., Primo, E.N., and Franco, A.A. (2020). Data-driven assessment of electrode calendaring process by combining experimental results, in silico mesostructures generation and machine learning. *J. Power Sources* 480, 229103.
23. Marks, D.S., Colwell, L.J., Sheridan, R., Hopf, T.A., Pagnani, A., Zecchina, R., and Sander, C. (2011). Protein 3D structure computed from evolutionary sequence variation. *PLoS One* 6.
24. Deep neural networks for object detection | Proceedings of the 26th International Conference on Neural Information Processing Systems - Volume 2 <https://dl.acm.org/doi/10.5555/2999792.2999897>.
25. Yang, M., Wang, S., Bakita, J., Vu, T., Smith, F.D., Anderson, J.H., and Frahm, J.M. (2019). Re-thinking CNN frameworks for time-sensitive autonomous-driving applications: Addressing an industrial challenge. In *Proceedings of the IEEE Real-Time and Embedded Technology and Applications Symposium, RTAS* (Institute of Electrical and Electronics

Engineers Inc.), pp. 305–317.

26. Yue, S. (2017). Imbalanced Malware Images Classification: a CNN based Approach. arXiv.
27. Barth, R., Hemming, J., and Van Henten, E.J. (2018). Improved Part Segmentation Performance by Optimising Realism of Synthetic Images using Cycle Generative Adversarial Networks.
28. Wei, H., Zhao, S., Rong, Q., and Bao, H. (2018). Predicting the effective thermal conductivities of composite materials and porous media by machine learning methods. *Int. J. Heat Mass Transf.* *127*, 908–916.
29. Rabbani, A., and Babaei, M. (2019). Hybrid pore-network and lattice-Boltzmann permeability modelling accelerated by machine learning. *Adv. Water Resour.* *126*, 116–128.
30. Benediktsson, J.A., Pesaresi, M., and Arnason, K. (2003). Classification and feature extraction for remote sensing images from urban areas based on morphological transformations. *IEEE Trans. Geosci. Remote Sens.* *41*, 1940–1949.
31. Alqahtani, N., Alzubaidi, F., Armstrong, R.T., Swietojanski, P., and Mostaghimi, P. (2020). Machine learning for predicting properties of porous media from 2d X-ray images. *J. Pet. Sci. Eng.* *184*, 106514.
32. Sudakov, O., Burnaev, E., and Koroteev, D. (2018). Driving Digital Rock towards Machine Learning: predicting permeability with Gradient Boosting and Deep Neural Networks. *Comput. Geosci.* *127*, 91–98.
33. Deringer, V.L. (2020). Modelling and understanding battery materials with machine-learning-driven atomistic simulations. *J. Phys. Energy* *2*, 041003.
34. Usseglio-Viretta, F.L.E., and Smith, K. (2017). Quantitative Microstructure Characterization of a NMC Electrode. *ECS Trans.* *77*, 1095–1118.
35. Holzer, L., Muench, B., Wegmann, M., Gasser, P., and Flatt, R.J. (2006). FIB-Nanotomography of Particulate Systems—Part I: Particle Shape and Topology of Interfaces. *J. Am. Ceram. Soc.* *89*, 2577–2585.
36. Chouchane, M., Rucci, A., and Franco, A.A. (2019). A Versatile and Efficient Voxelization-Based Meshing Algorithm of Multiple Phases. *ACS Omega* *4*, 11141–11144.
37. Torayev, A., Rucci, A., Magusin, P.C.M.M., Demortière, A., De Andrade, V., Grey, C.P., Merlet, C., and Franco, A.A. (2018). Stochasticity of Pores Interconnectivity in Li-O₂ Batteries and its Impact on the Variations in Electrochemical Performance. *J. Phys. Chem. Lett.* *9*, 791–797.
38. Torayev, A., Magusin, P.C.M.M., Grey, C.P., Merlet, C., and Franco, A.A. (2018). Importance of Incorporating Explicit 3D-Resolved Electrode Mesostructures in Li-O₂ Battery Models. *ACS Appl. Energy Mater.* *1*, 6433–6441.

39. Khan, Z.A., Salaberri, P.A.G., Heenan, T.M.M., Jervis, R., Shearing, P.R., Brett, D., Elkamel, A., and Gostick, J.T. (2020). Probing the Structure-Performance Relationship of Lithium-Ion Battery Cathodes Using Pore-Networks Extracted from Three-Phase Tomograms. *J. Electrochem. Soc.* *167*, 40528.
40. Latt, J., Malaspinas, O., Kontaxakis, D., Parmigiani, A., Lagrava, D., Brogi, F., Belgacem, M. Ben, Thorimbert, Y., Leclaire, S., Li, S., et al. (2020). Palabos: Parallel Lattice Boltzmann Solver. *Comput. Math. with Appl.*
41. Harris, C.R., Millman, K.J., van der Walt, S.J., Gommers, R., Virtanen, P., Cournapeau, D., Wieser, E., Taylor, J., Berg, S., Smith, N.J., et al. (2020). Array programming with NumPy. *Nature* *585*, 357–362.
42. Sullivan, C., and Kaszynski, A. (2019). PyVista: 3D plotting and mesh analysis through a streamlined interface for the Visualization Toolkit (VTK). *J. Open Source Softw.* *4*, 1450.
43. Masters, T., New, S.D., and Boston, Y. *Practical Neural Network Recipes in C++*.
44. Saltelli, A. (2002). Making best use of model evaluations to compute sensitivity indices. *Comput. Phys. Commun.* *145*, 280–297.
45. Gan, Y., Duan, Q., Gong, W., Tong, C., Sun, Y., Chu, W., Ye, A., Miao, C., and Di, Z. (2014). A comprehensive evaluation of various sensitivity analysis methods: A case study with a hydrological model. *Environ. Model. Softw.* *51*, 269–285.
46. Nadeina, A., Rozier, P., and Seznec, V. (2020). Facile Synthesis of a Common Na-Ion Battery Cathode Material $\text{Na}_3\text{V}_2(\text{PO}_4)_2\text{F}_3$ by Spark Plasma Sintering. *Energy Technol.* *8*, 1901304.
47. Maurel, A., Armand, M., Grugeon, S., Fleutot, B., Davoisne, C., Tortajada, H., Courty, M., Panier, S., and Dupont, L. (2020). Poly(Ethylene Oxide)–LiTFSI Solid Polymer Electrolyte Filaments for Fused Deposition Modeling Three-Dimensional Printing. *J. Electrochem. Soc.* *167*, 070536.